Crystal growth and quantum oscillations in the topological chiral semimetal CoSi

Xitong Xu,[1] Xirui Wang,[1] Tyler A. Cochran,[2] Daniel S. Sanchez,[2] Guoqing Chang,[2] Ilya Belopolski,[2] Guangqiang Wang,[1] Yiyuan Liu,[1] Hung-Ju Tien,[3] Xin Gui,[4] Weiwei Xie,[4] M. Zahid Hasan,[2,5] Tay-Rong Chang,[3,6] and Shuang Jia[1,7,8,9,*]

[1]*International Center for Quantum Materials, School of Physics, Peking University, Beijing 100871, China*

[2]*Laboratory for Topological Quantum Matter and Spectroscopy (B7), Department of Physics, Princeton University, Princeton, New Jersey 08544, USA*

[3]*Department of Physics, National Cheng Kung University, Tainan 701, Taiwan*

[4]*Department of Chemistry, Louisiana State University, Baton Rouge, Louisiana 70803, USA*

[5]*Lawrence Berkeley National Laboratory, Berkeley, California 94720, USA*

[6]*Center for Quantum Frontiers of Research and Technology (QFort), Tainan 701, Taiwan*

[7]*Collaborative Innovation Center of Quantum Matter, Beijing 100871, China*

[8]*CAS Center for Excellence in Topological Quantum Computation, University of Chinese Academy of Sciences, Beijing 100190, China*

[9]*Beijing Academy of Quantum Information Sciences, West Building 3, No. 10 Xibeiwang East Road, Haidian District, Beijing 100193,China*

(Received 30 March 2019; published 8 July 2019)

We survey the electrical transport properties of single-crystalline, topological chiral semimetal CoSi grown via different methods. High-quality CoSi single crystals were found in the growth from a tellurium solution. The sample's high carrier mobility enables us to observe quantum oscillations (QOs) in its thermoelectrical signals. Our analysis of QOs reveals two spherical Fermi surfaces around the R point in its Brillouin zone corner. The extracted Berry phases of these electron orbits are consistent with the -2 chiral charge as reported in density functional theory (DFT) calculations. A detailed analysis of the QOs reveals that the spin-orbit-coupling-induced band splitting is less than 2 meV near the Fermi level, one order of magnitude smaller than our DFT calculation. We also report a large phonon-drag-induced Nernst effect in CoSi at intermediate temperatures.

DOI: 10.1103/PhysRevB.100.045104

I. INTRODUCTION

Topological materials have been a hot research frontier since the discovery of topological insulators and semimetals [1–4]. Fundamental fermionic particles in high-energy physics, including Majorana, Dirac, and Weyl fermions [5], exist in momentum space as low-energy quasiparticle excitations in these materials' electronic bands. One example is the Weyl semimetal, which features linear crossings of two nondegenerate bands [4,6–10]. These band crossings, dubbed spin-1/2 Weyl nodes, can be described by a topological charge, i.e., a quantized Chern number $|C| = 1$. The Weyl node necessitates the presence of exotic helicoid surface states and Fermi arcs. Recent theories in condensed-matter physics have expanded the zoo of quasiparticles with no counterparts in the standard model. These unconventional fermions can be classified into two groups: (1) higher-fold chiral fermions with quantized nonzero Chern numbers, including the three-, four-, and sixfold chiral fermions [11–14], and (2) nonchiral multifold fermions, such as eightfold double Dirac fermions [15], threefold nexus fermions [16–18], and other nonchiral threefold- and sixfold-degenerate fermions [11].

Cobalt monosilicide crystalizes in a chiral structure in the $P2_13$ space group [Fig. 1(a), inset]. It has been intensely studied as a potential thermoelectric material [19–24] due to its large power factor at room temperature. Recent theoretical work has found that all pointlike degeneracies in the momentum space of structural chiral crystals are chiral fermions [12]. Among them, CoSi and its isostructural sibling RhSi possess a sixfold-degenerate chiral fermion at the R point and a fourfold-degenerate chiral fermion at the Γ point in their Brillouin zones (BZs) [13,14,25]. These chiral fermions with large topological charges are connected by long, robust Fermi arcs on the surface which were later confirmed by angle-resolved photoemission spectroscopy (ARPES) experiments [26–28]. However, no transport properties of CoSi directly related to its topological nature have been reported until now. As far as we are aware, previous reported CoSi single crystals manifest relatively low carrier mobilities, and no quantum oscillation (QO) has been observed in their electrical properties under magnetic field. The low sample quality makes it difficult to bridge the transport properties with its topological band structure.

Here we report our crystal growth and a survey of the electrical transport properties of single-crystalline CoSi. Tellurium was found to be an appropriate metal flux for the growth of CoSi which yields high-quality single crystals with large magnetoresistance (MR) and carrier mobilities. Although there is plenty of research work on the thermopower of CoSi [19–24,29–33], few studies have paid attention to its magneto-Seebeck and Nernst effects. Combining the high quality of our Te-flux-grown samples and the sensitivity of the thermoelectricity measurement [34], we are able to observe QOs in the thermoelectric signals of CoSi. By analyzing the QOs in magneto-Seebeck and Nernst signals at different

*gwljiashuang@pku.edu.cn

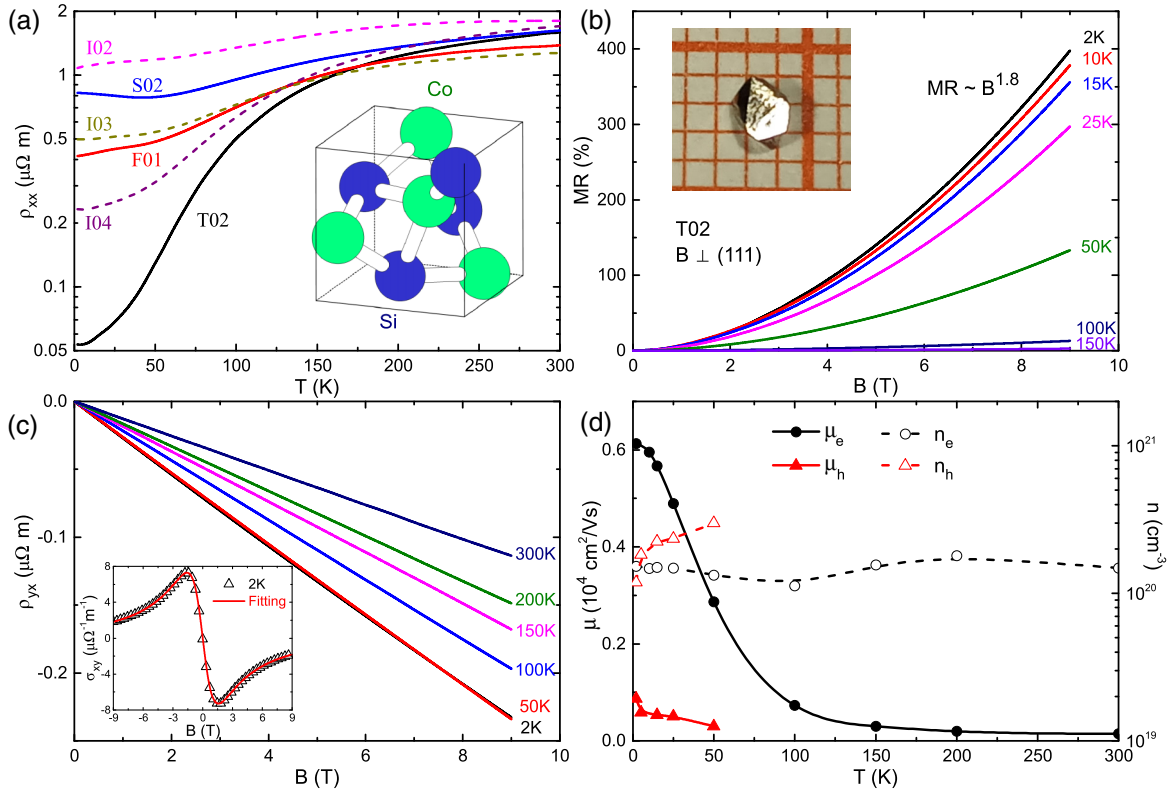

FIG. 1. (a) $\rho(T)$ curves of selected CoSi crystals with RRR ranging from 1.7 to around 30 (see Table I). Note the log scale of ρ_{xx}. Inset: Unit cell of CoSi. (b) MR of sample T02 at different temperatures. Inset: A photo of the Te-flux-grown crystal revealing shiny (111) facets. (c) Hall resistivity of T02. Inset: Two-band fitting of the Hall conductivity. (d) The mobilities and concentrations of electrons and holes in T02 at different temperatures.

temperatures and magnetic field directions, we reveal two spherical Fermi surfaces around the BZ corner R point, which is consistent with our density functional theory (DFT) calculations. The extracted Berry phases of the electron orbit equal zero, agreeing well with the scenario of -2 chiral charge at the R point. We also found that the spin-orbit coupling (SOC)-induced band splitting is less than 2 meV near the Fermi level, and this result is one order smaller than our DFT calculations. Moreover, we report a large Nernst effect in CoSi due to the combination of high mobility and the phonon-drag contribution at intermediate temperatures. As a consequence, a relatively large Nernst-Ettingshausen figure of merit ZT_ϵ [35] of around 0.03 is achieved at 42 K in 14 T.

II. METHOD

We used floating-zone, chemical vapor transport (CVT), and flux methods to grow CoSi single crystals successfully. In the floating-zone growth, polycrystalline CoSi was first prepared by arc melting stoichiometric cobalt and silicon chunks, and then the crystal was grown in a Quantum Design 2-Mirror IR Image Furnace. In the standard CVT method, either CoSi powder or fresh cobalt and silicon powder was used as starting materials. About 1 g of raw material, together with transport agent I_2 or Br_2, was loaded into a fused silica tube which was 22 cm in length and 1 cm in inner diameter. The tube was then sealed in vacuum, and the transport reaction was maintained at high temperatures for around 10 days. Shiny, millimeter-sized polyhedronlike crystals were yielded. Antimony, tin, and tellurium were chosen as the liquid solution in the flux growth. In the growth from tellurium flux, cobalt, silicon, and tellurium powder with a molar ratio of 1:1:20 were set in an alumina crucible and then sealed in a fused silica ampoule in vacuum. After soaking at 1050 °C for a few hours, the ampule was slowly cooled down to the centrifuging temperature of 700 °C at the rate of 3 °C/h. Several single-crystalline chunks developing large (111) facets were obtained. A similar procedure was carried out in antimony and tin flux growth, but the resulting rodlike crystals were smaller. Detailed information is summarized in Table I.

Electrical properties of as-obtained CoSi crystals were mainly characterized in a Quantum Design physical property measurement system (PPMS-9). Thermoelectric measurement was carried out in a 14-T Oxford Teslatron PT system, using a one-heater-two-thermometer setup in which the temperature gradient was applied within the crystallographic (111) plane and magnetic field $\boldsymbol{H}$ was applied perpendicular to the plane. Vacuum better than 3×10^{-5} Pa was maintained during the measurement. The thermoelectric voltage signals were amplified by using EM DC Amplifier A10 and subsequently collected in a Keithley 2182A nanovoltmeter. Thermal conductivity was measured simultaneously. Angle-dependent Nernst signals were measured in a rotating probe in the same magnet in which the vacuum was kept at around 10^{-3} Pa for the effective heat sink of the probe. ARPES measurements were carried out at the Advanced Resonant

TABLE I. Summary of the electrical transport properties of the CoSi single crystals from different growth conditions. Electric current was applied in the basal plane. μ_e and n_e are the estimated mobility and concentration of electrons at 2 K. For CVT growth, the material was transported from T_1 to T_2.

Sample	Basal plane	RRR	MR_{9T} (%)	μ_e ($cm^2/V\,s$)	n_e ($10^{20}cm^{-3}$)	Growth condition
F01		3.33	5	640	1.92	Floating zone
I01	(111)	1.63	−1.4	280	1.05	CVT, Co+Si+0.1 g I_2, 900 °C to 1100 °C
I02	(111)	1.67	−1.2	350	1.29	CVT, Co+Si+0.1 g I_2, 900 °C to 1100 °C
I04	(110)	7.33	29	1300	1.49	CVT, Co+Si+0.1 g I_2, 900 °C to 1100 °C
I03		2.56	1.7	410	2.42	CVT, Co+Si+5 mg I_2, 900 °C to 1000 °C
I05	(100)	8.32	34.9	2050	2.87	CVT, CoSi+5 mg I_2, 1000 °C to 1100 °C
B01	(111)	2.87	−0.4			CVT, Co+Si+1.5 mL Br_2, 1100 °C to 900 °C
B02	(110)	1.66	−4			CVT, Co+Si+1.5 mL Br_2, 1100 °C to 900 °C
S01		1.61	4.8			Flux, CoSi+19Sb, 1300 °C to 750 °C
S02		1.97	9.8	230	3.02	Flux, CoSi+19Sb, 1050 °C to 700 °C
T01	(111)	19.9	314	7300	2.55	Flux, Co+Si+20Te, 1050 °C to 700 °C
T02	(111)	29.5	398	6300	1.47	Flux, Co+Si+20Te, 1050 °C to 700 °C

Spectroscopies (ADRESS) beamline of the Swiss Light Source using a SPECS PHOIBIOS 150 analyzer. Natural facets of CoSi single crystals were Ar sputtered and annealed *in situ* in ultrahigh vacuum before being measured at 13 K. Spectra were acquired using 550 eV right circular and left circular incident photons with an energy resolution of 85 meV and angular resolution <0.07°. Right and left circular spectra were summed to eliminate the significant effect of circular dichroism. Band structure calculations were performed under the framework of the generalized gradient approximation of DFT [36] as implemented in the VASP package [37]. A lattice parameter of 4.450 Å was used for CoSi.

III. EXPERIMENTAL RESULTS AND DISCUSSION

The room-temperature resistivity of our CoSi samples generally ranges from 1 to 2 $\mu\Omega\,m$, close to previously reported values for both poly- and single-crystalline CoSi [24,31,38–40]. All the samples show metallic temperature-dependent resistivity $\rho(T)$ in Fig. 1(a), but their residual resistance ratios [RRRs, defined as the ratio of $R(300\ K)/R(2\ K)$] differ from each other. We notice that the $\rho(T)$ curves of the crystals grown via the CVT method have apparent sample dependence; for example, the RRRs of samples I02 and I04, which were grown in the same conditions, differed by four times (see Table I). Moreover, the $\rho(T)$ curves of the samples with a small RRR tends to have an upturn feature below 50 K, while their MR at 9 T is negative and small (Table I). These features indicate large magnetic defect concentrations in the samples with a small RRR [39].

In this study we focus on the single crystals grown from tellurium flux. These crystals are about 2 mm in size and are prone to develop large (111) planes. No residual Te was found within the accuracy of energy dispersive spectroscopy. These crystals have the largest RRR (∼30) reported for CoSi to our knowledge, and hereafter, we focus on sample T02.

The quasiquadratic profile of MR ($\propto B^{1.8}$) for sample T02 [Fig. 1(b)] is similar to that observed in arc-melted samples [40], but the value is larger (MR = 400% at 2 K in 9 T). Yet the MR is still smaller than those of typical Dirac and Weyl semimetals [41–44], indicating relatively low carrier mobilities. The Hall resistivity measurement shows a negative, nearly linear field dependence [Fig. 1(c)], and the slope remains unchanged below 50 K. We fit the off-diagonal conductivity tensor by using a two-band model [45],

$$\sigma_{xy} = \left[n_e\mu_e^2 \frac{1}{1+(\mu_e B)^2} - n_h\mu_h^2 \frac{1}{1+(\mu_h B)^2} \right] eB,$$

where n_e (n_h) and μ_e (μ_h) denote the carrier concentration and mobility of electrons (holes) and $e = -|e|$ is the electron charge hereafter for clarity. Above 50 K, a simple one-carrier model is used to estimate the concentration and mobility of electrons because of the small MR. As shown in Fig. 1(d), the carrier concentration of both electrons and holes is around $1.5 \times 10^{20}\,cm^{-3}$ at 2 K, while the mobility of electrons (∼6000$cm^2/V\,s$) is much larger than that of holes. This is reasonable due to the fact that hole carriers in CoSi are much heavier than electrons [19,32]. The electron concentration remains intact in the whole temperature range, while the mobility drops abruptly above 50 K, reflecting a significant reduction of the mean free path of the carriers at higher temperature. The mobility of holes also drops rapidly with temperature, being less than 300 $cm^2/V\,s$ at 50 K. The low mobility of the holes verifies the rationality of adopting a single-band approximation above 50 K.

Figures 2(a) and 2(b) show S_{xx} and S_{xy} of sample T02 at low temperatures. Strong QOs with an apparent beating pattern are observed in both S_{xx} and S_{xy} at base temperature, which indicates that there exist two oscillatory parts close in magnitude and frequency. Although the QOs quickly damp with increasing temperature, this beating feature and relative phase remain unchanged. Our fast Fourier transformation (FFT) reveals two fundamental frequencies of 568 and 671 T in Fig. 2(d), labeled as the α and β orbits, respectively.

To extract the cyclotron masses of the orbits, we analyze the QOs at different temperatures. The temperature dependence of the QOs on resistivity and magnetization is well described by the Lifshitz-Kosevich (LK) formula [46] as follows:

$$R_T = \frac{\alpha pX}{\sinh \alpha pX} = D(\mathbb{X}),$$

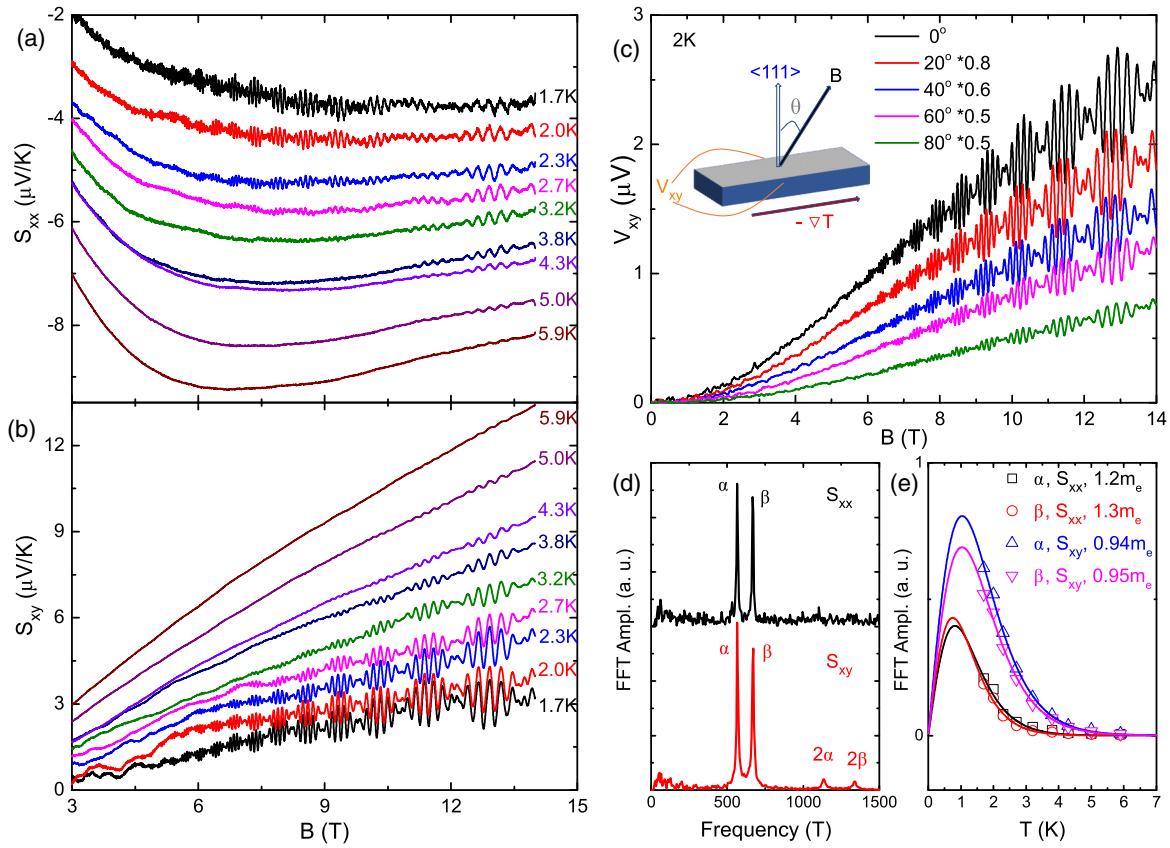

FIG. 2. (a) and (b) Magnetothermopower S_{xx} and S_{xy} at selected temperatures. The magnetic field is along the crystallographic [111] orientation. (c) Nernst voltages at selected angles when the magnetic field is tilted within the plane expanded by the [111] direction and the direction of the temperature gradient. Note that the voltages have been multiplied by some coefficients for clarity. (d) FFT spectra of S_{xx} and S_{xy}. (e) Fitting of cyclotron mass m^* using the derivative of the LK formula.

where $\alpha = 2\pi^2 k_B/e\hbar$, $X = m^*T/B$, m^* is the cyclotron mass, and $\mathbb{X} = \alpha pX$. Previous works pioneered by Fletcher and colleagues [47–52] suggest that the thermal damping factor for the diffusive part of the magnetothermopower should be

$$R_T = |D'(\mathbb{X})| = \frac{(\alpha pX)\coth(\alpha pX) - 1}{\sinh(\alpha pX)}$$

as the QOs in S_{ij} depend on the derivative of the density of states. Note that there is no apparent contribution to QOs from phonon drag below 10 K because the carrier density of CoSi is high and the Fermi surface is large. Moreover, there is no drift of the oscillatory phases at different temperatures. The cyclotron masses of α and β are fitted to be $1.2m_e$ and $1.3m_e$ in S_{xx} and 0.94 and 0.95 in S_{xy}, respectively. These cyclotron masses, close to previously reported effective masses of electrons ($\sim 2m_e$) in CoSi [19,32], are much heavier than those of electrons observed in the Weyl semimetal TaAs family [42,43,53]. The difference between cyclotron masses obtained from S_{xx} and S_{xy} deserves better understanding in the future.

In order to map the Fermi surface in the momentum space, we also performed Nernst voltage measurements with the magnetic field along different orientations. The field is laid in the plane expanded by the crystallographic [111] direction and $-\nabla T$ [Fig. 2(c)]. Aside from the relative magnitude, the oscillatory pattern of the Nernst voltages remains almost unchanged over the whole 2π angle. This result suggests that the two Fermi surfaces involved are spherical.

Before we proceed with the analysis of the Berry phases of these two orbits, the criterion for numbering the Landau index has to be clarified in the thermoelectric measurements. A previous study selected the peak positions of the oscillatory part of S_{xx} as integral Landau indices (note that here the integral corresponds to the Fermi level leaving the Nth Landau level) and further included the additional phase from the thermoelectrical measurement [54]. The criterion for detecting the Landau indices in S_{xy} is more complicated [55]. Yet this practice for S_{xx} seems invalid in CoSi. As shown in Fig. 3(a), ΔS_{xx} and ΔS_{xy} are antiphase for the mean frequency below 10 T, and the beating patterns are in phase. Above 11 T, the mean frequency changes to in phase, but the phase shift of the beating patterns cannot be resolved.

To solve this paradox we go back to the definition of $\boldsymbol{S}$. In an infinite medium, the total current density in the presence of a temperature gradient and magnetic field can be formulated [56] as

$$\boldsymbol{J} = \boldsymbol{\sigma} \cdot \boldsymbol{E} - \boldsymbol{\epsilon} \cdot \nabla T,$$

where $\boldsymbol{\epsilon}$ is the thermoelectric tensor. By definition, $S_{ij} = E_i/\nabla_j T$, and $\boldsymbol{S} = \boldsymbol{\rho} \cdot \boldsymbol{\epsilon}$. For the oscillatory part (denoted by

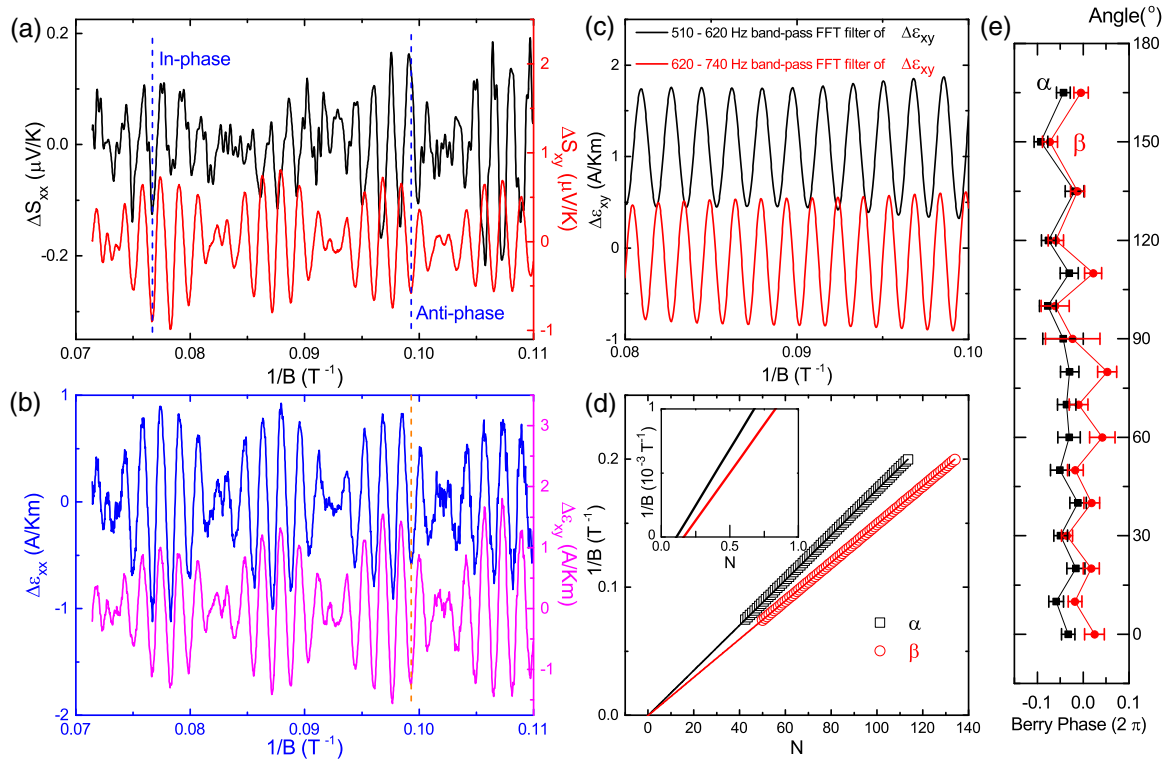

FIG. 3. (a) Oscillatory part of S_{xx} and S_{xy} at 1.7 K. Note the different scales. (b) Oscillatory part of the thermoelectric tensors ϵ_{xx} and ϵ_{xy}. (c) $\Delta\epsilon_{xy}$ after passing the bandpass FFT filter. (d) Landau fan diagram. Peak positions in (c) are assigned integral values, while valley positions are assigned half integrals. Inset: Close-up near $N = 0$. (e) Angle dependence of extracted Berry phases from V_{xy}. The error bar is set to be 3 times the value of the standard deviation.

the tilde) in $\boldsymbol{\epsilon}$, Fletcher and colleagues have given a simple formula [47–50]:

$$\widetilde{\boldsymbol{\epsilon}} = \mp i\frac{\pi k_B}{e}\frac{D'(\mathbb{X})}{D(\mathbb{X})}\widetilde{\boldsymbol{\sigma}} = \beta\widetilde{\boldsymbol{\sigma}},$$

with the upper sign (negative) for electrons (note that here we neglect the contribution from the nondiffusive part again and $\widetilde{\boldsymbol{\sigma}}$ is not necessarily observable). Note the negative sign in e and $D'(\mathbb{X})$, and $\beta = \mp i|\beta|$ for electrons and holes, respectively. The above formula should hold water at least in the relatively low field and low temperature region, as it is actually inferred from the well-known Mott relation [56]. It is easy to get the form

$$\widetilde{\boldsymbol{S}} \simeq \beta\bar{\boldsymbol{\rho}}\cdot\widetilde{\boldsymbol{\sigma}},$$

where $\bar{\boldsymbol{\rho}}$ denotes the nonoscillatory part of the resistivity tensor. For the metals where $\bar{\rho}_{xx} \gg \bar{\rho}_{yx}$, e.g., ZrSiS [54], it is safe to use $\widetilde{S}_{xx} \simeq \beta\bar{\rho}_{xx}\widetilde{\sigma}_{xx}$. However, $\bar{\rho}_{xx}$ and $\bar{\rho}_{yx}$ are of the same magnitude in our CoSi sample; therefore, the diagonal and off-diagonal parts get entangled in S_{ij}. Remember $\widetilde{\boldsymbol{\sigma}}$ is linked to the oscillatory part of the density of states $\widetilde{g}$ [49],

$$\widetilde{\sigma}_{xx} \propto \frac{\sigma_0}{1+\omega_c^2\tau_0^2}\frac{\widetilde{g}}{g_0}, \quad \widetilde{\sigma}_{xy} \propto \frac{\sigma_0}{(1+\omega_c^2\tau_0^2)\omega_c\tau_0}\frac{\widetilde{g}}{g_0},$$

where ω_c is the cyclotron frequency $|e|B/m^*$, τ is the quantum lifetime, and the subscript 0 denotes the value at zero field. For electronlike bands, $\widetilde{\sigma}_{xx}$ and $\widetilde{\sigma}_{xy}$ are in phase. As $\widetilde{S}_{xy}$ approximately equals $\beta(\bar{\rho}_{xx}\widetilde{\sigma}_{xy} - \bar{\rho}_{yx}\widetilde{\sigma}_{xx})$, $\widetilde{S}_{xy}$, $\widetilde{\epsilon}_{xx}$, and $\widetilde{\epsilon}_{xy}$ should be in phase and have an additional $-i$ phase with respect to $\widetilde{g}$. As $\widetilde{S}_{xx}$ approximates $\beta(\bar{\rho}_{xx}\widetilde{\sigma}_{xx} + \bar{\rho}_{yx}\widetilde{\sigma}_{xy})$, the phase is actually dependent on the relative magnitude of $\bar{\rho}_{xx}\widetilde{\sigma}_{xx}$ and $-\bar{\rho}_{yx}\widetilde{\sigma}_{xy}$. For holes, similar results are expected, except that $\widetilde{\epsilon}_{xx}$ and $\widetilde{\epsilon}_{xy}$ have a $+i$ phase with respect to $\widetilde{g}$, while $\widetilde{S}_{xy}$ has an additional $-i$ phase.

We plot the oscillatory parts of ϵ_{ij} in Fig. 3(b), in comparison with the oscillatory parts of S_{ij} in Fig. 3(a). Apparently, the phases of $\widetilde{S}_{xy}$, $\widetilde{\epsilon}_{xx}$, and $\widetilde{\epsilon}_{xy}$ are perfectly in phase, which again indicates that these oscillations stem from electronlike pockets.

Because there exist only two distinct frequencies in QOs, we are able to separate them thoroughly using the FFT filter, as shown in Fig. 3(c) for $\Delta\epsilon_{xy}$. No signs of Zeeman splitting are found due to the small SOC strength and limited field range of our experiments. The peak positions are assigned integral Landau indices, while the valley positions are assigned half integrals. Using the so-called Landau fan diagram [Fig. 3(d)], we extract phases of 0.11 and 0.16 for α and β, respectively. The total phase shift ϕ_s equals $-1/2 + \phi_B + \phi_{3D} + \phi_T$, where ϕ_B is the Berry phase, ϕ_T is $-1/4$ (namely, $-i$) here for electrons in thermoelectric QOs, and the additional phase shift ϕ_{3D} stemming from the dispersion along k_z equals $-1/8$ for a maximum cross section of electrons [57]. We finally get the Berry phases for α and β as -0.015 and 0.035, respectively. The angle dependence of the Berry phases is also obtained from the Nernst voltage measurement when the field is along different orientations. As shown in Fig. 3(e),

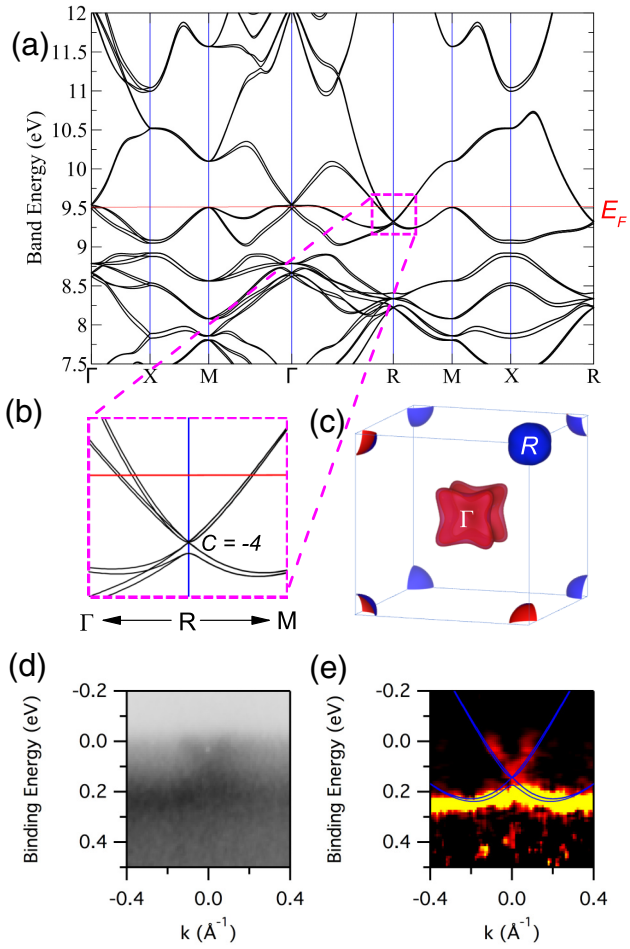

FIG. 4. (a) Band structure of CoSi when SOC is included. (b) Close-up around the R point. (c) Calculated Fermi surfaces of CoSi. (d) ARPES spectra and (e) curvature plot of a double Weyl fermion at the R point. Blue lines are band calculation results with 30 meV downward shift of the Fermi energy.

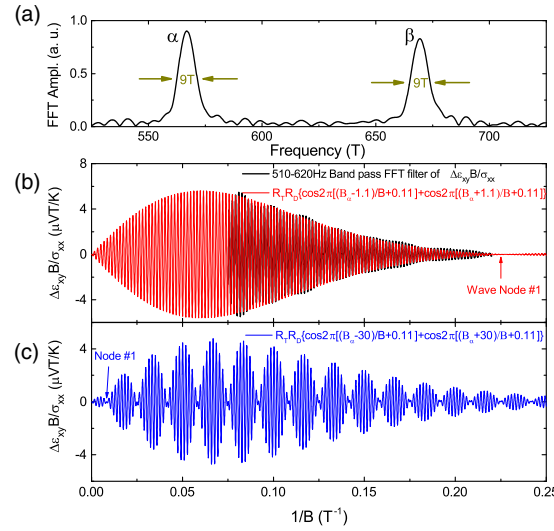

FIG. 5. (a) FFT spectrum of $\Delta\epsilon_{xy}$. The FWHMs for both α and β pockets are around 9 T. (b) $\Delta\epsilon_{xy}B/\sigma_{xx}$ after passing a 510–620-Hz band FFT filter. The coefficient B/σ_{xx} is used for the conformity to the LK formula. The red line is a simulation using two frequencies close to B_α (567 and 569 T). (c) A simulation using two frequencies estimated from DFT calculation ($B_\alpha \pm 30$T) in comparison to (b).

the Berry phases are close to zero over the whole 2π angle for these two pockets.

We now compare our results to the DFT-calculated band structure and ARPES experimental results. The DFT calculation shows electronlike pockets centered at the R point in the BZ corner and holelike pockets at the Γ point in the BZ center [Fig. 4(a)]. The hole pockets around Γ stem from a rather flat band and are too large and heavy for transport experiments to detect. The crossing point at M happens to be very close to the Fermi energy and is sensitive to calculation parameters. In Ref. [26], this band crossing point is slightly higher than E_F, while it is a bit below E_F in Ref. [14]. We comment that as the hole mobilities in the CoSi sample are fairly small, it is hard to determine from transport experiments alone whether there are hole pockets around M. At the R point, when SOC is neglected, a band crossing with fourfold degeneracy occurs 180 meV below the Fermi level. This is a double Weyl fermion with a Chern number of -2 [13,14,25]. Our ARPES experiment demonstrates the double Weyl fermion at the R point but is unable to resolve the α and β branches due to instrumental energy resolution [Figs. 4(d) and 4(e)].

Our measured oscillatory frequencies (568 and 671 T) match the DFT calculation without SOC (574 and 660 T) very well if the Fermi level is shifted down by about 30 meV. The Fermi energy E_F of the electron pockets is estimated via $E_F = \hbar^2 k_F^2/m^*$, averaging around 160–140 meV (using m^* from S_{xy}), which is consistent with the DFT calculation. We also estimated the carrier concentrations for electrons from the QOs by using the equation $n_{QO} = k_F^3/6\pi^2$. For the α and β pockets, the densities are 3.82×10^{19} and 4.90×10^{19} cm^{-3}, respectively. Considering the spin degeneracy, the total electron density is estimated as 1.74×10^{20} cm^{-3}, close to the value obtained from the two-band model (1.47×10^{20} cm^{-3} for electrons).

When SOC is included in the DFT calculation, a chiral sixfold-degenerate double spin-1 Weyl node carrying a -4 topological charge is formed at the R point. This Weyl node hosts Fermi surfaces of two pairs of near-spherical concentric sheets with different spin textures but similar sizes. As Co and Si are light elements, the SOC strength is actually small, and therefore, the band splitting is of the order of 10 meV near the Fermi level [13]. Our DFT calculation shows that each pair of Fermi surfaces should have a 10% difference in the extremal cross-section areas within the (111) plane due to SOC-induced splitting. In comparison we observed only two spin-degenerate orbits (α and β) in the QOs.

We now estimate the upper limit of the SOC-induced band splitting in our measurements. As shown in Fig. 5(a), the full widths at half maximum (FWHMs) for both α and β pockets are around 9 T, which sets an upper limit of the difference between the SOC-split orbits. To address a more acute upper limit, we consider the detailed profile of the FFT filtered oscillation [Fig. 5(b)]. If we assume that B_α is composed of two close frequencies similar in magnitude, the interference of the two oscillations will create wave nodes in the oscillatory

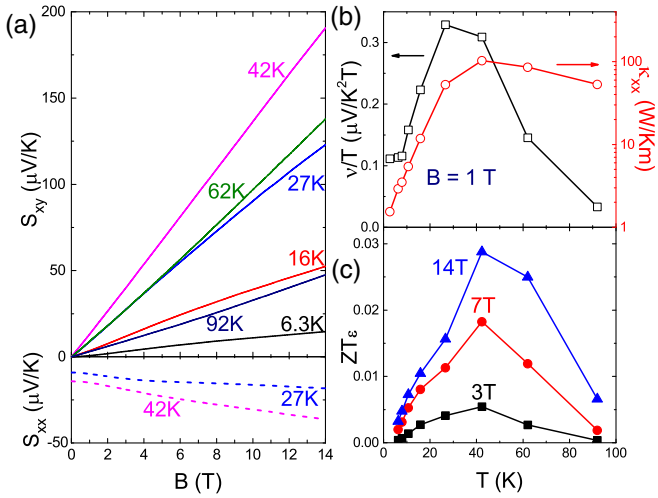

FIG. 6. (a) S_{xy} and S_{xx} of T02 at higher temperatures. (b) Nernst coefficient divided by temperature (ν/T) and thermal conductivity κ_{xx} at 1 T. (c) Nernst-Ettingshausen figure of merit ZT_ϵ under different magnetic fields.

spectrum. As there is no phase inversion in the bandpass FFT filter in the field range of our measurement, we conclude that the first wave node appears at least after 0.22 T^{-1} [Fig. 5(b)]. This gives the limitation of less than 2.2 T for the separation of the two frequencies induced by SOC. By comparison, the DFT with SOC expects a difference of around 60 T in the (111) plane, which will generate a more complicated pattern with multiple wave nodes within the observable field range [Fig. 5(c)]. The same results hold for the β orbit. Our analyses reveal that the SOC strength at the Fermi level is one order of magnitude smaller than what is expected by DFT. The SOC-induced energy split along Γ-R near the Fermi level should be less than 2 meV even when thermal broadening and Zeeman splitting are considered. This one order of magnitude larger SOC splitting of the DFT results, together with the previously discussed 30 meV discrepancy in Fermi energy to match the frequencies of QOs, may arise from the accuracy of the structural and correlation parameters in the calculation. Hubbard correction has been considered in RhSi in the Supplemental Material of Ref. [13] and would surely slightly modify the band structure.

Last, we consider the phonon-drag effect in CoSi at intermediate temperatures. As shown in Fig. 6(a), S_{xy} has a linear dependence on magnetic field over 6 to 100 K and shows no sign of saturation at 14 T. At 42 K, S_{xy} attains a maximum of around 190 μV/K in 14 T. By contrast, S_{xx} is much smaller under the same magnetic field. A large S_{xy} was explained as a result of a small Fermi energy and large carrier mobility [58,59]. In the low-field limit, the diffusive Nernst coefficient ν for electrons can be formulated [51,58,59] as

$$\nu/T = S_{xy}/BT = -\frac{\pi^2}{3}\frac{k_B}{e}\frac{k_B}{\epsilon_F}p\mu,$$

where $p = (\frac{\partial ln\tau}{\partial ln\epsilon})|_{\epsilon_F}$, a value usually close to unity [34]. Using the mobility and Fermi energy from our transport data, we have $\nu/T \sim 0.1p\ \mu V/K^2$ T at 6 K, which is quite close to our observation in Fig. 6(b). The ν/T increases rapidly with increasing temperature and peaks around 40 K, which suggests an additional large phonon-drag contribution at intermediate temperatures. Although thermal conductivity also peaks in the same region, a large $ZT_\epsilon = S_{xy}^2 T/\rho\kappa = 0.03$ is achieved at 42 K in 14 T. This value surpasses the ZT of pristine CoSi at room temperature and is comparable to those of hole-doped samples [22]. Noticing the necessity of a strong magnetic field, we suggest possible thermoelectric application of CoSi below liquid-nitrogen temperature.

IV. CONCLUSION

We reported on high-quality single crystals of the topological chiral semimetal CoSi grown from tellurium flux. The single crystals have large carrier mobilities, which enabled us to observe QOs in the thermoelectrical signals. The oscillatory frequencies reveal two spherical Fermi surfaces around the BZ corner R point, and our measurements suggest that the SOC strength in CoSi is one order of magnitude smaller than the DFT calculation, which may be related to the accuracy of the structural and correlation parameters in the calculation. The extracted Berry phases of these electron orbits agree well with the scenario of -2 chiral charge at R. In addition, we reported a relatively large ZT_ϵ of 0.03 in CoSi at 42 K in 14 T due to the high mobility and phonon-drag contribution. Our tellurium flux method might be feasible for growing high-quality crystals of other transition-metal silicides, like the Kondo insulator FeSi and the helimagnet MnSi. Our findings also highlight the potentials of magnetothermoelectric measurement for detecting high-frequency QOs in topological semimetals [60].

ACKNOWLEDGMENTS

This work was supported by the National Natural Science Foundation of China Grants No. U1832214 and No.11774007, the National Key R&D Program of China (Grant No. 2018YFA0305601), and the Strategic Priority Research Program of the Chinese Academy of Sciences (Grant No. XDB28000000). T.-R.C. was supported by the Young Scholar Fellowship Program of the Ministry of Science and Technology (MOST) in Taiwan under MOST Grant for the Columbus Program No. MOST108-2636-M-006-002, National Cheng Kung University, Taiwan, and the National Center for Theoretical Sciences (NCTS), Taiwan. This work is supported partially by MOST, Taiwan, Grant No. MOST 107-2627-E-006-001. Work at Princeton and Princeton-led ARPES measurements were supported by the U.S. Department of Energy under Basic Energy Sciences (Grant No. DOE/BES DE-FG-02-05ER46200). M.Z.H. acknowledges visiting scientist support from Lawrence Berkeley National Laboratory. The authors thank V. Strokov for support at the ADRESS beamline of the Swiss Light Source at the Paul Scherrer Institute in Switzerland. W.X. at LSU was supported by a Beckman Young Investigator award. X.G. at LSU is supported by the National Science Foundation under Grant No. NSF-OIA-1832967.

[1] M. Z. Hasan and C. L. Kane, Colloquium: Topological insulators, Rev. Mod. Phys. **82**, 3045 (2010).

[2] X.-L. Qi and S.-C. Zhang, Topological insulators and superconductors, Rev. Mod. Phys. **83**, 1057 (2011).

[3] Y. Ando, Topological insulator materials, J. Phys. Soc. Jpn. **82**, 102001 (2013).

[4] A. Burkov, Topological semimetals, Nat. Mater. **15**, 1145 (2016).

[5] P. B. Pal, Dirac, Majorana, and Weyl fermions, Am. J. Phys. **79**, 485 (2011).

[6] S. Jia, S.-Y. Xu, and M. Z. Hasan, Weyl semimetals, Fermi arcs and chiral anomalies, Nat. Mater. **15**, 1140 (2016).

[7] B. Yan and C. Felser, Topological materials: Weyl semimetals, Annu. Rev. Condens. Matter Phys. **8**, 337 (2017).

[8] A. Burkov, Weyl metals, Annu. Rev. Condens. Matter Phys. **9**, 359 (2018).

[9] S.-Y. Xu, I. Belopolski, N. Alidoust, M. Neupane, G. Bian, C. Zhang, R. Sankar, G. Chang, Z. Yuan, C.-C. Lee, S.-M. Huang, H. Zheng, J. Ma, D. S. Sanchez, B. Wang, A. Bansil, F. Chou, P. P. Shibayev, H. Lin, S. Jia, and M. Z. Hasan, Discovery of a Weyl fermion semimetal and topological Fermi arcs, Science **349**, 613 (2015).

[10] B. Q. Lv, H. M. Weng, B. B. Fu, X. P. Wang, H. Miao, J. Ma, P. Richard, X. C. Huang, L. X. Zhao, G. F. Chen, Z. Fang, X. Dai, T. Qian, and H. Ding, Experimental Discovery of Weyl Semimetal TaAs, Phys. Rev. X **5**, 031013 (2015).

[11] B. Bradlyn, J. Cano, Z. Wang, M. G. Vergniory, C. Felser, R. J. Cava, and B. A. Bernevig, Beyond Dirac and Weyl fermions: Unconventional quasiparticles in conventional crystals, Science **353**, aaf5037 (2016).

[12] G. Chang, B. J. Wieder, F. Schindler, D. S. Sanchez, I. Belopolski, S.-M. Huang, B. Singh, D. Wu, T.-R. Chang, T. Neupert, S.-Y. Xu, H. Lin, and M. Z. Hasan, Topological quantum properties of chiral crystals, Nat. Mater. **17**, 978 (2018).

[13] G. Chang, S.-Y. Xu, B. J. Wieder, D. S. Sanchez, S.-M. Huang, I. Belopolski, T.-R. Chang, S. Zhang, A. Bansil, H. Lin, and M. Z. Hasan, Unconventional Chiral Fermions and Large Topological Fermi Arcs in RhSi, Phys. Rev. Lett. **119**, 206401 (2017).

[14] P. Tang, Q. Zhou, and S.-C. Zhang, Multiple Types of Topological Fermions in Transition Metal Silicides, Phys. Rev. Lett. **119**, 206402 (2017).

[15] B. J. Wieder, Y. Kim, A. M. Rappe, and C. L. Kane, Double Dirac Semimetals in three Dimensions, Phys. Rev. Lett. **116**, 186402 (2016).

[16] H. Weng, C. Fang, Z. Fang, and X. Dai, Topological semimetals with triply degenerate nodal points in θ-phase tantalum nitride, Phys. Rev. B **93**, 241202(R) (2016).

[17] Z. Zhu, G. W. Winkler, Q. S. Wu, J. Li, and A. A. Soluyanov, Triple Point Topological Metals, Phys. Rev. X **6**, 031003 (2016).

[18] G. Chang, S.-Y. Xu, S.-M. Huang, D. S. Sanchez, C.-H. Hsu, G. Bian, Z.-M. Yu, I. Belopolski, N. Alidoust, H. Zheng, T.-R. Chang, H.-T. Jeng, S. A. Yang, T. Neupert, H. Lin, and M. Z. Hasan, Nexus fermions in topological symmorphic crystalline metals, Sci. Rep. **7**, 1688 (2017).

[19] S. Asanabe, D. Shinoda, and Y. Sasaki, Semimetallic properties of $Co_{1-x}Fe_xSi$ solid solutions, Phys. Rev. **134**, A774 (1964).

[20] M. Fedorov and V. Zaitsev, Semimetals as materials for thermoelectric generators, in *CRC Handbook of Thermoelectrics* (CRC Press, Boca Raton, FL, 1995), p. 299.

[21] S. Kim, Y. Mishima, and D. Choi, Effect of process conditions on the thermoelectric properties of CoSi, Intermetallics **10**, 177 (2002).

[22] C. S. Lue, Y.-K. Kuo, C. L. Huang, and W. J. Lai, Hole-doping effect on the thermoelectric properties and electronic structure of CoSi, Phys. Rev. B **69**, 125111 (2004).

[23] W. Ren, C. Li, L. Zhang, K. Ito, and J. Wu, Effects of Ge and B substitution on thermoelectric properties of CoSi, J. Alloy. Compd. **392**, 50 (2005).

[24] E. Skoug, C. Zhou, Y. Pei, and D. T. Morelli, High thermoelectric power factor in alloys based on CoSi, Appl. Phys. Lett. **94**, 022115 (2009).

[25] D. A. Pshenay-Severin, Y. V. Ivanov, A. A. Burkov, and A. T. Burkov, Band structure and unconventional electronic topology of CoSi, J. Phys.: Condens. Matter **30**, 135501 (2018).

[26] D. S. Sanchez, I. Belopolski, T. A. Cochran, X. Xu, J.-X. Yin, G. Chang, W. Xie, K. Manna, V. Süß, C.-Y. Huang, N. Alidoust, D. Multer, S. S. Zhang, N. Shumiya, X. Wang, G.-Q. Wang, T.-R. Chang, C. Felser, S.-Y. Xu, S. Jia, H. Lin, and M. Z. Hasan, Topological chiral crystals with helicoid-arc quantum states, Nature (London) **567**, 500 (2019).

[27] D. Takane, Z. Wang, S. Souma, K. Nakayama, T. Nakamura, H. Oinuma, Y. Nakata, H. Iwasawa, C. Cacho, T. Kim, K. Horiba, H. Kumigashira, T. Takahashi, Y. Ando, and T. Sato, Observation of Chiral Fermions with a Large Topological Charge and Associated Fermi-Arc Surface States in CoSi, Phys. Rev. Lett. **122**, 076402 (2019).

[28] Z. Rao, H. Li, T. Zhang, S. Tian, C. Li, B. Fu, C. Tang, L. Wang, Z. Li, W. Fan, J. Li, Y. Huang, Z. Liu, Y. Long, C. Fang, H. Weng, Y. Shi, H. Lei, Y. Sun, T. Qian, and H. Ding, Observation of unconventional chiral fermions with long Fermi arcs in CoSi, Nature (London) **567**, 496 (2019).

[29] H. Sun, X. Lu, and D. T. Morelli, Effects of Ni, Pd, and Pt substitutions on thermoelectric properties of CoSi alloys, J. Electron. Mater. **42**, 1352 (2013).

[30] H. Sun, X. Lu, and D. T. Morelli, Isovalent substitutes play in different ways: Effects of isovalent substitution on the thermoelectric properties of $CoSi_{0.98}B_{0.02}$, J. Appl. Phys. **120**, 035107 (2016).

[31] A. Burkov, S. Novikov, V. Zaitsev, and H. Reith, Transport properties of cobalt monosilicide and its alloys at low temperatures, Semiconductors **51**, 689 (2017).

[32] D. A. Pshenay-Severin, Yu. V. Ivanov, A. T. Burkov, S. V. Novikov, V. K. Zaitsev, and H. Reith, Electronic structure and thermoelectric properties of transition metal monosilicides, J. Electron. Mater. **47**, 3277 (2018).

[33] D. Pshenay-Severin, Y. Ivanov, and A. Burkov, The effect of energy-dependent electron scattering on thermoelectric transport in novel topological semimetal CoSi, J. Phys.: Condens. Matter **30**, 475501 (2018).

[34] K. Behnia, *Fundamentals of Thermoelectricity* (Oxford University Press, Oxford, 2015).

[35] G. S. Nolas, J. Sharp, and J. Goldsmid, *Thermoelectrics: Basic Principles and New Materials Developments*, Springer Series in Materials Science, Vol. 45 (Springer, Berlin, 2013).

[36] J. P. Perdew, K. Burke, and M. Ernzerhof, Generalized Gradient Approximation Made Simple, Phys. Rev. Lett. **77**, 3865 (1996).

[37] G. Kresse and J. Furthmüller, Efficiency of *ab-initio* total energy calculations for metals and semiconductors using a plane-wave basis set, Comput. Mater. Sci. **6**, 15 (1996).

[38] A. E. Petrova, V. N. Krasnorussky, A. A. Shikov, W. M. Yuhasz, T. A. Lograsso, J. C. Lashley, and S. M. Stishov, Elastic, thermodynamic, and electronic properties of MnSi, FeSi, and CoSi, Phys. Rev. B **82**, 155124 (2010).

[39] S. M. Stishov, A. E. Petrova, V. A. Sidorov, and D. Menzel, Self-doping effects in cobalt silicide CoSi: Electrical, magnetic, elastic, and thermodynamic properties, Phys. Rev. B **86**, 064433 (2012).

[40] S. S. Samatham, D. Venkateshwarlu, and V. Ganesan, Investigations on pseudogap semimetal CoSi, Mater. Res. Express **1**, 026503 (2014).

[41] L. P. He, X. C. Hong, J. K. Dong, J. Pan, Z. Zhang, J. Zhang, and S. Y. Li, Quantum Transport Evidence for the Three-Dimensional Dirac Semimetal Phase in Cd_3As_2, Phys. Rev. Lett. **113**, 246402 (2014).

[42] C.-L. Zhang, Z. Yuan, Q.-D. Jiang, B. Tong, C. Zhang, X. C. Xie, and S. Jia, Electron scattering in tantalum monoarsenide, Phys. Rev. B **95**, 085202 (2017).

[43] C.-L. Zhang, S.-Y. Xu, C. Wang, Z. Lin, Z. Du, C. Guo, C.-C. Lee, H. Lu, Y. Feng, S.-M. Huang *et al.*, Magnetic-tunnelling-induced Weyl node annihilation in TaP, Nat. Phys. **13**, 979 (2017).

[44] M. N. Ali, J. Xiong, S. Flynn, J. Tao, Q. D. Gibson, L. M. Schoop, T. Liang, N. Haldolaarachchige, M. Hirschberger, N. Ong *et al.*, Large, non-saturating magnetoresistance in WTe_2, Nature (London) **514**, 205 (2014).

[45] C. Hurd, *The Hall Effect in Metals and Alloys* (Springer, Berlin, 2012).

[46] D. Shoenberg, *Magnetic Oscillations in Metals* (Cambridge University Press, Cambridge, 2009).

[47] R. Fletcher, On the amplitude of the quantum oscillations in the thermopower of metals, J. Low Temp. Phys. **43**, 363 (1981).

[48] R. Fletcher, Experimental investigation of the amplitudes of the quantum oscillations in the transport coefficients of Al, Phys. Rev. B **28**, 1721 (1983).

[49] P. T. Coleridge, R. Stoner, and R. Fletcher, Low-field transport coefficients in $GaAs/Ga_{1-x}Al_xAs$ heterostructures, Phys. Rev. B **39**, 1120 (1989).

[50] R. Fletcher, P. T. Coleridge, and Y. Feng, Oscillations in the diffusion thermopower of a two-dimensional electron gas, Phys. Rev. B **52**, 2823 (1995).

[51] B. Tieke, R. Fletcher, J. C. Maan, W. Dobrowolski, A. Mycielski, and A. Wittlin, Magnetothermoelectric properties of the degenerate semiconductor HgSe:Fe, Phys. Rev. B **54**, 10565 (1996).

[52] A. Palacio Morales, A. Pourret, G. Knebel, G. Bastien, V. Taufour, D. Aoki, H. Yamagami, and J. Flouquet, Thermoelectric power quantum oscillations in the ferromagnet UGe_2, Phys. Rev. B **93**, 155120 (2016).

[53] C.-L. Zhang, B. Tong, Z. Yuan, Z. Lin, J. Wang, J. Zhang, C.-Y. Xi, Z. Wang, S. Jia, and C. Zhang, Signature of chiral fermion instability in the Weyl semimetal TaAs above the quantum limit, Phys. Rev. B **94**, 205120 (2016).

[54] M. Matusiak, J. Cooper, and D. Kaczorowski, Thermoelectric quantum oscillations in ZrSiS, Nat. Commun. **8**, 15219 (2017).

[55] B. Fauqué, N. P. Butch, P. Syers, J. Paglione, S. Wiedmann, A. Collaudin, B. Grena, U. Zeitler, and K. Behnia, Magnetothermoelectric properties of Bi_2Se_3, Phys. Rev. B **87**, 035133 (2013).

[56] J. M. Ziman, *Electrons and Phonons: The Theory of Transport Phenomena in Solids* (Oxford University Press, Oxford, 2001).

[57] C. Li, C. M. Wang, B. Wan, X. Wan, H.-Z. Lu, and X. C. Xie, Rules for Phase Shifts of Quantum Oscillations in Topological Nodal-Line Semimetals, Phys. Rev. Lett. **120**, 146602 (2018).

[58] K. Behnia and H. Aubin, Nernst effect in metals and superconductors: A review of concepts and experiments, Rep. Prog. Phys. **79**, 046502 (2016).

[59] K. Behnia, M.-A. Méasson, and Y. Kopelevich, Nernst Effect in Semimetals: The Effective Mass and the Figure of Merit, Phys. Rev. Lett. **98**, 076603 (2007).

[60] X. Xu, Z. Kang, T.-R. Chang, H. Lin, G. Bian, Z. Yuan, Z. Qu, J. Zhang, and S. Jia, Quantum oscillations in the noncentrosymmetric superconductor and topological nodal-line semimetal $PbTaSe_2$, Phys. Rev. B **99**, 104516 (2019).